

Specificity of TGF- β 1 signal designated by LRRC33 and integrin $\alpha_v\beta_8$

Received: 24 February 2022

Accepted: 3 August 2022

Published online: 25 August 2022

Check for updates

Zelin Duan^{1,6}, Xuezhen Lin^{2,6}, Lixia Wang^{2,6}, Qiuxin Zhen¹, Yuefeng Jiang¹, Chuxin Chen¹, Jing Yang¹, Chia-Hsueh Lee³, Yan Qin⁴, Ying Li², Bo Zhao²✉, Jianchuan Wang⁵✉ & Zhe Zhang¹✉

Myeloid lineage cells present the latent form of transforming growth factor- β 1 (L-TGF- β 1) to the membrane using an anchor protein LRRC33. Integrin $\alpha_v\beta_8$ activates extracellular L-TGF- β 1 to trigger the downstream signaling functions. However, the mechanism designating the specificity of TGF- β 1 presentation and activation remains incompletely understood. Here, we report cryo-EM structures of human L-TGF- β 1/LRRC33 and integrin $\alpha_v\beta_8$ /L-TGF- β 1 complexes. Combined with biochemical and cell-based analyses, we demonstrate that LRRC33 only presents L-TGF- β 1 but not the - β 2 or - β 3 isoforms due to difference of key residues on the growth factor domains. Moreover, we reveal a 2:2 binding mode of integrin $\alpha_v\beta_8$ and L-TGF- β 1, which shows higher avidity and more efficient L-TGF- β 1 activation than previously reported 1:2 binding mode. We also uncover that the disulfide-linked loop of the integrin subunit β_8 determines its exquisite affinity to L-TGF- β 1. Together, our findings provide important insights into the specificity of TGF- β 1 signaling achieved by LRRC33 and integrin $\alpha_v\beta_8$.

Transforming growth factor- β (TGF- β) is a pleiotropic cytokine with indispensable roles in extensive physiological processes such as organ development, immune response, and tissue homeostasis^{1–4}. Dysregulation of TGF- β signaling is associated with many pathological conditions, e.g., cancer, autoimmune disease, fibrosis, and neurodegeneration^{5–7}. Therefore, in-depth knowledge of TGF- β signaling mechanism is vital for understanding the body's health and disease.

TGF- β is synthesized as a latent form (L-TGF- β) containing a 25-kDa N-terminal latency-associated peptide (LAP) and a 12-kDa C-terminal growth factor (mTGF- β) domain. L-TGF- β is folded as a homodimer in the endoplasmic reticulum and cleaved between LAP and mTGF- β by furin or furin-type proteases in the trans-Golgi network or the extracellular matrix⁸. Notably, LAP remains non-covalently associated with mTGF- β after cleavage, which prevents mTGF- β from

binding to TGF- β receptors^{8,9}. During biosynthesis, LAP is often covalently linked with specific anchor proteins through disulfide bonds. One class of such anchor proteins are latent TGF- β binding proteins (LTBPs), which deposit L-TGF- β to the extracellular matrix^{10,11}. Additionally, two leucine-rich repeat-containing anchor proteins, LRRC32 (also known as GARP) and LRRC33 (NRROS), present L-TGF- β on the plasma membrane of regulatory T (T_{reg}) cells and myeloid lineage cells (e.g., macrophages, dendritic cells, and microglia), respectively^{12–14}. Therefore, specific presentation and storage of L-TGF- β in different extracellular microenvironment by different anchor proteins serve as a critical regulatory mechanism of TGF- β signal in various biological contexts.

mTGF- β must be discharged from the LAP-anchor protein complex to activate the downstream signaling pathway, and multiple factors can trigger this activation process⁸. $\alpha_v\beta_6$ and $\alpha_v\beta_8$ integrins are the

¹State Key Laboratory of Membrane Biology, Center for Life Sciences, School of Life Sciences, Peking University, 100871 Beijing, China. ²Molecular Cancer Research Center, School of Medicine, Shenzhen Campus of Sun Yat-sen University, No. 66, Gongchang Road, Guangming District, 518107 Shenzhen, Guangdong, China. ³Department of Structural Biology, St. Jude Children's Research Hospital, Memphis, TN 38105, USA. ⁴Parthenon Therapeutics, 40 Guest street, Boston, MA 02135, USA. ⁵Center for Translational Research, Shenzhen Bay Laboratory, 518007 Shenzhen, Guangdong, China. ⁶These authors contributed equally: Zelin Duan, Xuezhen Lin, Lixia Wang. ✉ e-mail: zhaob39@mail.sysu.edu.cn; wangjc@szbl.ac.cn; zzhang01@pku.edu.cn

most well-established activators for L-TGF- β , which bind to the RGDXX(L/I) motif of LAP with nanomolar affinity^{15–17}. Integrin $\alpha_v\beta_6$ assists mTGF- β release by exerting tensile force to unfold LAP, and the attachment of L-TGF- β to the extracellular matrix or the cell surface by an anchor protein is required for such $\alpha_v\beta_6$ -mediated activation^{8,15}. In contrast, the mechanism of activation by integrin $\alpha_v\beta_8$ is still obscure. $\alpha_v\beta_8$'s lower affinity to L-TGF- β (~50-fold lower than that of $\alpha_v\beta_6$) and the absence of cytoskeleton attachment by the β_8 leg both suggest that $\alpha_v\beta_8$ is unable to transmit tensile force like $\alpha_v\beta_6$. Conformational changes of the L-TGF- β -anchor protein complex induced by $\alpha_v\beta_8$ binding likely facilitate other events leading to mTGF- β release^{18,19}.

Despite great scientific advances achieved in the TGF- β field, the underlying mechanism designating the specificity of TGF- β signal remains incompletely understood. In particular, three closely related isoforms of TGF- β (i.e., TGF- β_1 , β_2 , and β_3) are encoded in mammals. The growth factors of the three isoforms share 68% sequential identity and high structural similarity. These isoforms initiate essentially the same downstream signaling pathway, but they exhibit significantly different functions in physiology and disease^{1,20–22}. How is such functional distinction achieved remains to be determined.

In this work, we focus on the mechanism of specific L-TGF- β_1 presentation and activation mediated by LRRC33 and integrin $\alpha_v\beta_8$ in myeloid lineage cells. We report cryo-EM structure of the human L-TGF- β_1 /LRRC33 complex and demonstrate that LRRC33 can present only L-TGF- β_1 but not the β_2 or β_3 isoforms due to differences of key residues on their growth factor domains. Moreover, we uncover a specific binding mode between integrin $\alpha_v\beta_8$ and L-TGF- β_1 by solving a cryo-EM structure of 2:2 human integrin $\alpha_v\beta_8$ /L-TGF- β_1 complex which exhibits higher binding avidity and more efficient L-TGF- β_1 activation. Finally, we reveal that the disulfide-linked loop (DLL) of the integrin subunit β_8 determines its exquisite affinity to L-TGF- β_1 . These results offer crucial insights into the mechanism underlying the specificity of TGF- β_1 signaling.

Results

Structure of the human L-TGF- β_1 /LRRC33 complex

Human full-length L-TGF- β_1 (i.e., residues 1–361) and LRRC33 ectodomain (i.e., residues 1–631) were co-expressed in Expi293F cells (Fig. 1a). The secreted L-TGF- β_1 /LRRC33 complex was purified for cryo-EM analysis. The best subset of particles could be refined to 4.01-Å resolution (Fig. 1b, Supplementary Figs. 1, 2, and Table 1). Aided by the reported structures of L-TGF- β_1 ^{9,23} and L-TGF- β_1 /GARP²⁴, we built the structure model for the L-TGF- β_1 /LRRC33 complex (Fig. 1c). Both L-TGF- β_1 and LRRC33 have abundant N-linked glycosylation, which helps to validate this structural model (Supplementary Fig. 2e).

The LRR N-terminal region (RNT, residues 22–39) and seventeen LRR fragments (R1–R17, residues 40–501) of LRRC33 were mapped in the model (Fig. 1d). EM densities of the rest portion of LRRC33 appear discrete, implying the flexible nature of LRRs. LRRC33 adopts a classic solenoid structure of the leucine-rich repeat (LRR)-containing proteins. Superposition of LRRC33 and GARP shows a root-mean-square deviation (RMSD) of 3.89 Å for 309 C α atoms²⁴. In particular, the central region (R11–R15) of LRRC33 has an inward 3–5 Å movement (Fig. 1e). In addition, LRRC33 exhibits a 35-degree rotation compared to GARP²⁴ when bound to L-TGF- β_1 (Fig. 1f).

L-TGF- β_1 takes similar global structures in our L-TGF- β_1 /LRRC33 complex and the reported L-TGF- β_1 /GARP complex²⁴ (Fig. 1f and Supplementary Fig. 3a). LAP adopts a wreath shape to encircle the mTGF- β_1 dimer with ~3800 Å² buried interface area (Fig. 1a–c). The straitjacket of LAP is linked to the lateral side of LRRC33 via covalent bonds. The Cys4 residues in the α_1 helix from either LAP monomer form asymmetrical intermolecular disulfide bonds with Cys201 or Cys345 of LRRC33 (Fig. 1c, g, and h). The N-terminal region of LAP_A inserts into the hydrophobic core of LRRC33 from its convex side, facilitating the formation of the Cys4_A-Cys201 bond (Fig. 1g). In

contrast, the N-terminal region of LAP_B floats on the lateral surface of LRRC33 and further stabilizes their complex through van der Waals interactions (Fig. 1h). In addition to the covalent interaction, a non-covalent interface between LRRC33 and one mTGF- β_1 molecule (mTGF- β_{1B}) was also presented in our structure (Fig. 1i).

Compared to the previously reported structures^{9,15,23,24}, L-TGF- β_1 in its complex with LRRC33 displays three major local conformational characteristics. First, the α_3 helix and preceding loop (Pro296-His317) of mTGF- β_{1B} flip over to accommodate the non-covalent interaction with LRRC33, similar to that observed in the L-TGF- β_1 /GARP complex (Fig. 1j and Supplementary Fig. 3a). Second, the N-terminal region including the α_1 helix adopts a unique structure in our complex, suitable for disulfide bond formation with LRRC33 (Fig. 1k and Supplementary Fig. 3a). Third, the distal end of Arm domain, including the RGDXX(L/I) motif and bowtie region, exhibits structural plasticity in different L-TGF- β_1 structures, which might provide enough mobility for integrin recognition (Fig. 1l and Supplementary Fig. 3a).

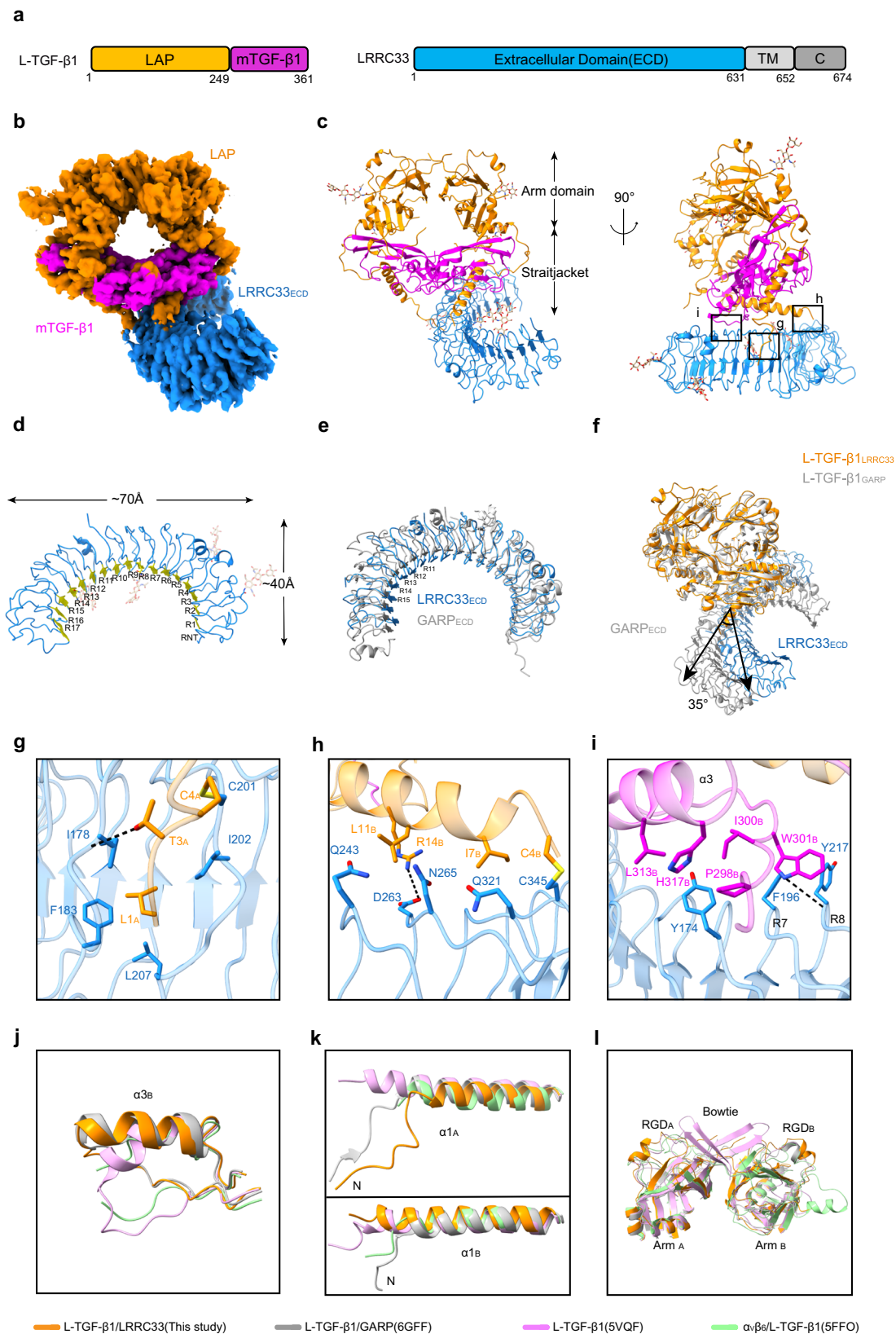
Non-covalent interface essential for L-TGF- β_1 /LRRC33

The anchor proteins LTBP1, GARP, and LRRC33 are covalently linked to L-TGF- β_1 via two disulfide bonds involving the conserved Cys4 residue of LAP^{14,24,25}. However, non-covalent interactions between different anchor proteins and L-TGF- β_1 are heterogeneous^{25–28}. In our structure, mTGF- β_{1B} leans onto the lateral surface of LRRC33, resulting in a non-covalent interface of 535 Å² (Fig. 1i). Trp301 of mTGF- β_{1B} inserts into a groove of LRRC33 between LRR fragments R7 and R8, forming hydrophobic interactions with Phe196 and Tyr217 of LRRC33, as well as hydrogen bond with the main-chain carboxyl group of Tyr217. At the same time, Tyr174 of LRRC33 is embedded into a hydrophobic pocket of mTGF- β_{1B} consisting of Pro298, Ile300, Leu313, and His317 (Fig. 1i and Supplementary Fig. 3b).

We next sought to determine the functional relevance of such extensive non-covalent interactions in the assembly of L-TGF- β_1 /LRRC33 complex by introducing mutations to the two key aromatic residues. Both the W301A mutation of L-TGF- β_1 and the Y174R mutation of LRRC33 drastically decreased the L-TGF- β_1 /LRRC33 complex formation and the cell-surface presentation of L-TGF- β_1 (Fig. 2a–c and Supplementary Fig. 4a). Y174R also impaired LRRC33's ability to withhold L-TGF- β_1 from secretion (Fig. 2c). These results demonstrated that non-covalent interaction is critical in the assembly of L-TGF- β_1 and LRRC33. Notably, unlike its homologous anchor protein GARP, LRRC33's cell-surface expression depends on the coexpression of L-TGF- β_1 (Supplementary Fig. 4b, c), suggesting that L-TGF- β_1 acts as a molecular chaperone for LRRC33 during biosynthesis.

LRRC33 specificity for L-TGF- β_1

Anchor proteins, such as LTBP and GARP, have been reported with different specificity for the three TGF- β isoforms^{8,13,29}. Our results showed that LRRC33 specifically presents L-TGF- β_1 , but not the β_2 or β_3 isoforms, to the plasma membrane (Fig. 2d and Supplementary Fig. 4d, e). In contrast, GARP efficiently presents all three isoforms (Supplementary Fig. 4f, g). The N-terminal Cys4 residue for covalent linkage to the anchor proteins is conserved in all three L-TGF- β isoforms, indicating the aforementioned non-covalent L-TGF- β_1 /LRRC33 interface is likely a key factor determining their specificity. We examined the regions surrounding the α_3 helix (Pro296-His317) of mTGF- β_{1B} that predominantly mediates the non-covalent interactions with LRRC33 (Fig. 2e, f). Non-conserved residues within this region were systematically replaced with cognate residues of the β_2 and β_3 isoforms. Mutating His317 to the cognate residue of β_2 (i.e., H317I) or β_3 (i.e., H317L) severely impaired L-TGF- β_1 presentation by LRRC33 (Fig. 2g and Supplementary Fig. 5a). Notably, such mutations did not affect L-TGF- β_1 secretion nor cell surface presentation by GARP, ruling out any potential issue of protein expression or folding (Supplementary Fig. 5a, b). In addition, we found substituting Lys309 to the



cognate residue of β3 (i.e., K309T) but not β2 (i.e., K309R) inhibited cell-surface presentation of L-TGF-β1 by LRRC33 (Fig. 2g and Supplementary Fig. 5a). Although the side-chain density of Lys309 in mTGF-β1_B is not directly visible in the L-TGF-β1/LRRC33 EM map, this residue likely participates in van der Waals interactions with Cys98 and Ser100 of LRRC33 based on the structural model (Supplementary Fig. 3c).

Trp301, one of the two aforementioned key residues for L-TGF-β1/LRRC33 non-covalent interaction, is conserved in β1 and β2 but not β3. Mutating Trp301 to the cognate residue of β3 (i.e., W301R) also affected the L-TGF-β1 recognition (Fig. 2g and Supplementary Fig. 5a), although to a lesser extent compared to the W301A mutation (Fig. 2a). This is probably due to the partially negatively charged surface of

Fig. 1 | Cryo-EM structure of the L-TGF- β 1/LRRC33 complex. **a** Sequence schematic diagrams of L-TGF- β 1 and LRRC33. Chromatic bricks represent the protein regions used in our study, whereas gray bricks represent regions that are not included. Latency-associated peptide (LAP), mature TGF- β 1 (mTGF- β 1), and the extracellular domain of LRRC33 (LRRC33_{EC}) are colored in orange, magenta, and blue, respectively. **b** Cryo-EM map of the L-TGF- β 1/LRRC33 complex. The contour level is 0.286. Individual domains are colored the same as those in **a**. **c** Overall structure of the L-TGF- β 1/LRRC33 complex in ribbon presentation. The color code is the same as before. The Arm and straitjacket domains are labeled. **d** Ribbon diagram of LRRC33. R1 to R17, leucine-rich repeat (LRR); RNT, LRR N-terminal

region. Yellow arrows represent the β strands in each repeat. **e** Superposition of individual LRRC33 and GARP (PDB code: 6GFF) from their complex structures with L-TGF- β 1. LRRC33 is colored in blue, and GARP is colored in gray. R11–R15 of LRRC33 are indicated. **f** Superposition of L-TGF- β 1/LRRC33 and L-TGF- β 1/GARP (PDB code: 6GFF) complexes according to L-TGF- β 1. Compared with GARP, LRRC33 rotates about 35 degrees relative to the diad axis of L-TGF- β 1 dimer. **g–i** Interaction details between L-TGF- β 1 and LRRC33 as indicated in the insets of **c**. Residues in different L-TGF- β 1 monomers are distinguished by subscripts A and B. Black dashed lines represent hydrogen bond interaction (<4 Å). **j–l** Comparison of three distinguishing regions in L-TGF- β 1 between our structure and others.

LRRC33 that surrounds the Trp301 residue of mTGF- β 1_B (Supplementary Fig. 3d).

To further validate the essential role of these three residues (Trp301, Lys309, and His317) for LRRC33 recognition, we introduced combined mutations in L-TGF- β 1 to the cognate residues of β 2 (H317I) or β 3 (W301R/K309T/H317L). Both mutations dramatically abolished the assembly of the L-TGF- β 1/LRRC33 complex (Fig. 2h, i and Supplementary Fig. 5c, d). In addition, reverse mutations back to the cognate residues of L-TGF- β 1 were introduced to L-TGF- β 2 or L-TGF- β 3. Strikingly, a single mutation of Ile350 on L-TGF- β 2 (i.e., I350H) was sufficient to restore its complex formation with LRRC33. Similarly, L-TGF- β 3 with triple mutations of Arg328, Thr336, and Lys344 (i.e., R328W/T336K/L344H) could also be recognized and presented by LRRC33 (Fig. 2h, i and Supplementary Fig. 5c, d). However, this L-TGF- β 3 variant did not fully recapitulate the binding of L-TGF- β 1, indicating that other residues/regions may be at play.

Specificity of the TGF- β 1 activation by integrin α _v β ₈

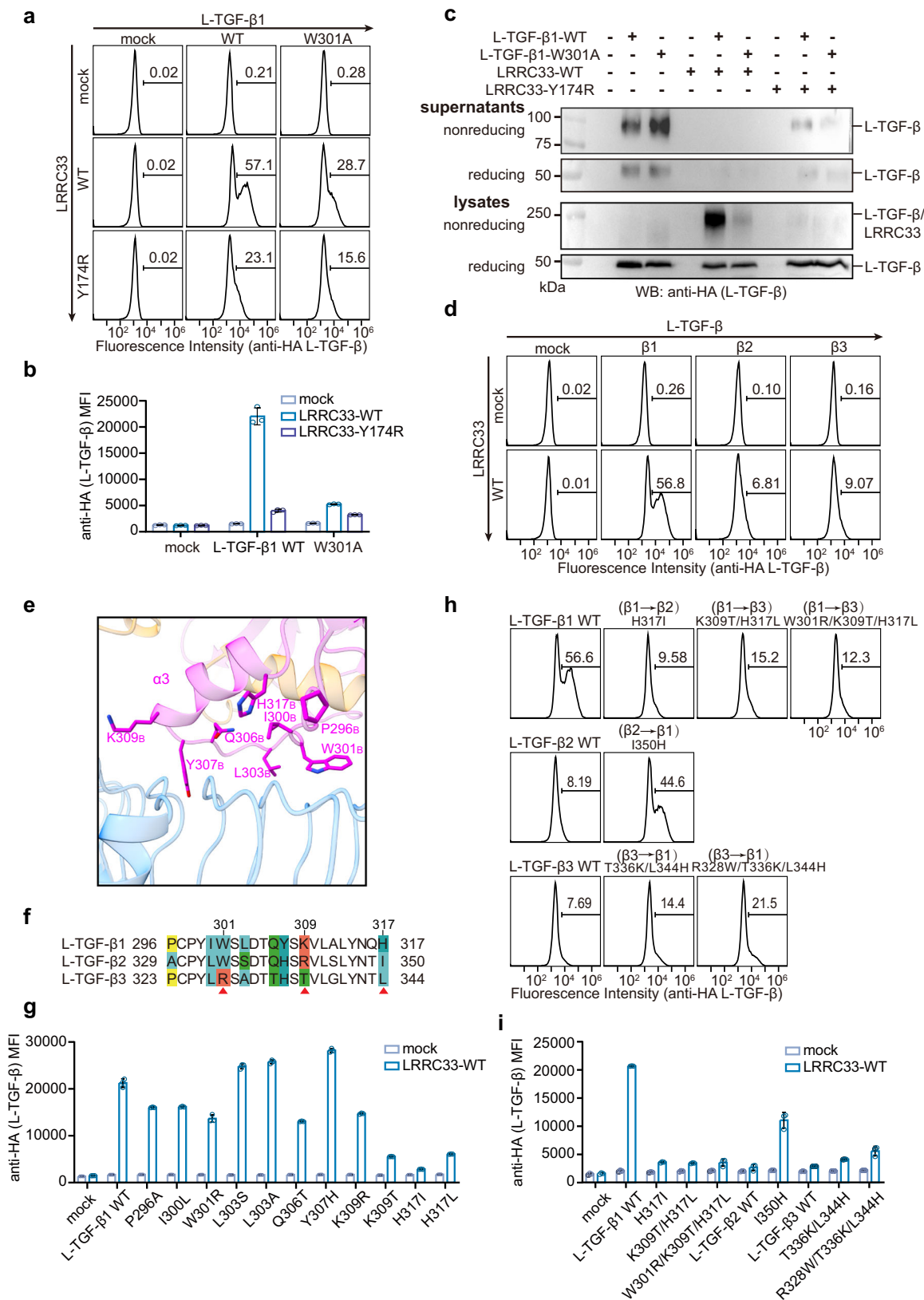
In contrast to integrin α _v β ₆ which is predominantly expressed in epithelial cells, α _v β ₈ is reported to be expressed in multiple immune cells that co-reside with L-TGF- β 1 expressing myeloid lineage cells and is highly relevant in immune regulation^{8,22}. Moreover, in the central nervous system (CNS), L-TGF- β 1/LRRC33 activation in microglia depends on α _v β ₈ but not α _v β ₆¹⁴. To reveal the recognition and activation mechanisms of L-TGF- β 1/LRRC33 by integrin α _v β ₈, we next sought to pursue the cryo-EM structure of the α _v β ₈/L-TGF- β 1/LRRC33 ternary complex. Integrin α _v β ₈ could bind L-TGF- β 1 either in a ratio of 1:2 or 2:2¹⁶. We used a α _v β ₈/L-TGF- β 1/LRRC33 ternary complex of 2:2:1 stoichiometry for structural determination, in which integrin α _v β ₈ contains only the headpiece involved in L-TGF- β 1 binding (i.e., residues 1–594 of α _v subunit and residues 1–456 of β ₈ subunit) (Fig. 3a). Due to structural flexibility¹⁹ and pseudo-symmetric property of the ternary complex, only a medium-resolution structure (~5 Å) was achieved (Supplementary Fig. 6). To understand the interactions between integrin α _v β ₈ and L-TGF- β 1, we focused on one α _v β ₈ headpiece and the L-TGF- β 1 dimer within the EM map. Exquisite 3D classification showed that the EM densities of L-TGF- β 1 and the relative position between α _v β ₈ and L-TGF- β 1 varied considerably between different subclasses, especially for the three classes with relatively higher resolution (Supplementary Fig. 7). This is in concert with the observed plasticity of L-TGF- β 1 in the reported α _v β ₈/L-TGF- β 1 structure¹⁹. The best subclass of our 1:2 α _v β ₈/L-TGF- β 1 complex was finally refined to a resolution of 3.24 Å (Supplementary Figs. 6, 8 and Table 1), where the head region of α _v β ₈ shows clear EM densities, including the β -propeller and proximal thigh domains of α _v subunit and the β I and hybrid domains of β ₈ subunit (Fig. 3b). In contrast to other integrins whose headpieces adopt an open conformation upon ligand binding³⁰, the α _v β ₈ headpiece remains closed in complex with L-TGF- β 1^{19,31} (Fig. 3b, c). The absence of a metal ion in the conserved adjacent to metal ion-dependent adhesion site (ADMIDAS)^{19,31} is observed in our α _v β ₈/L-TGF- β 1 structure (Supplementary Fig. 9a).

The structure of α _v β ₈ headpiece in our α _v β ₈/L-TGF- β 1 complex is almost identical to the reported ones either on its own or in complex with L-TGF- β 1^{19,31,32} (Supplementary Fig. 9b). In terms of L-TGF- β 1, the

entire integrin-binding regions were well resolved in the density map, allowing us to build the corresponding structure model (Fig. 3d). In our structure, the RGD tri-peptide (²¹⁵RGD²¹⁷) of L-TGF- β 1 inserts into the cleft between α _v β -propeller and β ₈ β I domains, similar to the reported α _v β ₈/L-TGF- β 1 and α _v β ₆/L-TGF- β 1 structures^{15,19,31}. However, the adjacent proximal loop (²⁰⁷INGFTTGR²¹⁴) and integrin-binding (IB) helix (²¹⁸LATIHGM²²⁴) of L-TGF- β 1 undergo tremendous conformational changes (Fig. 3e–g). Interestingly, rather than forming a continuous α -helix with ²¹⁸LATI²²¹, His222 of L-TGF- β 1 flips outward and disrupts the secondary structure of the IB helix. Thus, we refer to the conventional IB helix as IB loop in our structure (Fig. 3e). The rotation of His222 breaks its hydrogen bond with the main-chain carboxyl group of Asn211, which helps to maintain the conventional proximal loop and IB helix structures in the 1:2 α _v β ₈/L-TGF- β 1 complex¹⁹. Instead, in our 2:2 α _v β ₈/L-TGF- β 1 complex, His222 is stabilized by Thr87 and His88 of L-TGF- β 1, and His118 of integrin β ₈ through van der Waals interactions (Fig. 3f, g and Supplementary Fig. 9c). Moreover, Tyr172 of integrin β ₈ forms hydrogen bond with Thr212 to fix the proximal loop in the new position (Fig. 3f, g). This remodeling of proximal and IB loops of L-TGF- β 1 leads to the movement of RGD motif by -14 Å and the subsequent rotation of integrin α _v β ₈ by -60 degrees compared to the reported α _v β ₈/L-TGF- β 1 structure¹⁹ (Fig. 3h, i).

To obtain an intact structure model for the 2:2:1 α _v β ₈/L-TGF- β 1/LRRC33 complex, we fitted our α _v β ₈/L-TGF- β 1 and L-TGF- β 1/LRRC33 structures into the medium-resolution EM map of the ternary complex (Supplementary Fig. 6). These two structures could be well aligned based on the common L-TGF- β 1 component. A subsequent symmetric operation of the 1:2 α _v β ₈/L-TGF- β 1 model generated a 2:2 α _v β ₈/L-TGF- β 1 structure that nicely fits the EM map (Supplementary Fig. 9d), which helps confirm the structural model of the α _v β ₈/L-TGF- β 1/LRRC33 complex. This assembled model suggests that LRRC33 presents dimeric L-TGF- β 1 on the surface of one cell, and two adjacent α _v β ₈ molecules are able to bind L-TGF- β 1 simultaneously with an included angle of -80 degrees (Fig. 3j).

To explore the functional significance of the different binding stoichiometry between integrins and L-TGF- β 1 (1:2, one integrin bound to one L-TGF- β 1 dimer; and 2:2, two integrins simultaneously bound to one L-TGF- β 1 dimer) for TGF- β 1 activation, the following experiments were carried out. We made a mutant L-TGF- β 1 construct with abolished integrin-binding ability by mutating the ²¹⁵RGDLATI²²¹ motif to RGE-GATG (Supplementary Fig. 10a). Co-transfection of wild-type (WT) and mutant L-TGF- β 1 constructs would yield three types of L-TGF- β 1 dimer protein: WT L-TGF- β 1 dimer (capable of binding two integrins), chimeric L-TGF- β 1 dimer (capable of binding one integrin), and the mutant L-TGF- β 1 dimer (no integrin binding). By comparing integrin-induced TGF- β 1 activation of WT and chimeric L-TGF- β 1 dimers, we could distinguish the activation efficiency of different integrin-binding ratios (2:2 or 1:2). Constant amount of WT L-TGF- β 1 (25 ng) and GARP (500 ng) DNA were co-transfected with varied amount of mutant L-TGF- β 1 DNA (0–475 ng) into Expi293F cells to display L-TGF- β 1 onto the cell surface. Next, these cells were co-cultured with α _v β ₈-expressing cells, and the TGF- β 1 activity was measured using a transiently transfected (CAGA)₁₂-Luciferase reporter cell line³³. By gradually increasing the ratio of mutant to WT L-TGF- β 1 DNA in co-transfection



(0 ng:25 ng to 475 ng:25 ng), less WT L-TGF- β 1 dimers, and more chimeric and mutant L-TGF- β 1 dimers were displayed onto the cell surface (Supplementary Fig. 10b, c). Our results showed that, although the total amount of WT L-TGF- β 1 subunit remained the same, L-TGF- β 1 activation decreased gradually, suggesting that WT L-TGF- β 1 dimers with two integrin-binding arms have higher activation efficiency than

the chimeric dimer with only one integrin-binding arm (Fig. 4a and Supplementary Fig. 10b).

We speculated that the higher activation efficiency of the 2:2 binding mode is caused by the avidity effect. We integrated the Fc fragment of IgG₁ (IgG₁ Fc) to the C-terminal of integrin β ₃ subunit to tether two α _v β ₃ integrins in a heterotetramer form which is able to

Fig. 2 | Non-covalent interaction is essential for the L-TGF- β 1/LRRC33 assembly and determines L-TGF- β isoform specificity. **a** Surface L-TGF- β 1 (anti-HA) expressions on transfected Expi293F cells were measured by flow cytometry. Number in each histogram indicates the percentage of L-TGF- β + (anti-HA+) subset. **b** MFI (Mean Fluorescence Intensity) of L-TGF- β (anti-HA) on differently transfected Expi293F cells. All experiments were done in triplicate ($n = 3$ biologically independent experiments, mean \pm s.d.). **c** Culture supernatants and total lysates of Expi293F cells transfected with indicated plasmids were subjected to non-reducing and reducing immunoblot analyses with anti-HA antibody (for L-TGF- β). The experiment was repeated three times independently with similar results. **d** Surface presentations of different L-TGF- β isoforms by LRRC33 were measured by flow

cytometry. Number in each histogram indicates the percentage of L-TGF- β + (anti-HA+) subset. **e** The non-covalent interface between mTGF- β 1 and LRRC33. Side chains are shown for the mTGF- β 1 residues that are in close distance with LRRC33. **f** Sequence alignment of the potential LRRC33-binding regions of the three L-TGF- β isoforms. Non-conserved residues are colored. **g** Surface presentation (MFI) of different L-TGF- β 1 mutants by LRRC33. All experiments were done in triplicate ($n = 3$ biologically independent experiments, mean \pm s.d.). **h, i** Cross mutations of the three key residues between different L-TGF- β isoforms switch their LRRC33-binding specificity. All experiments were done in triplicate ($n = 3$ biologically independent experiments, mean \pm s.d.). Source data are provided as a Source Data file.

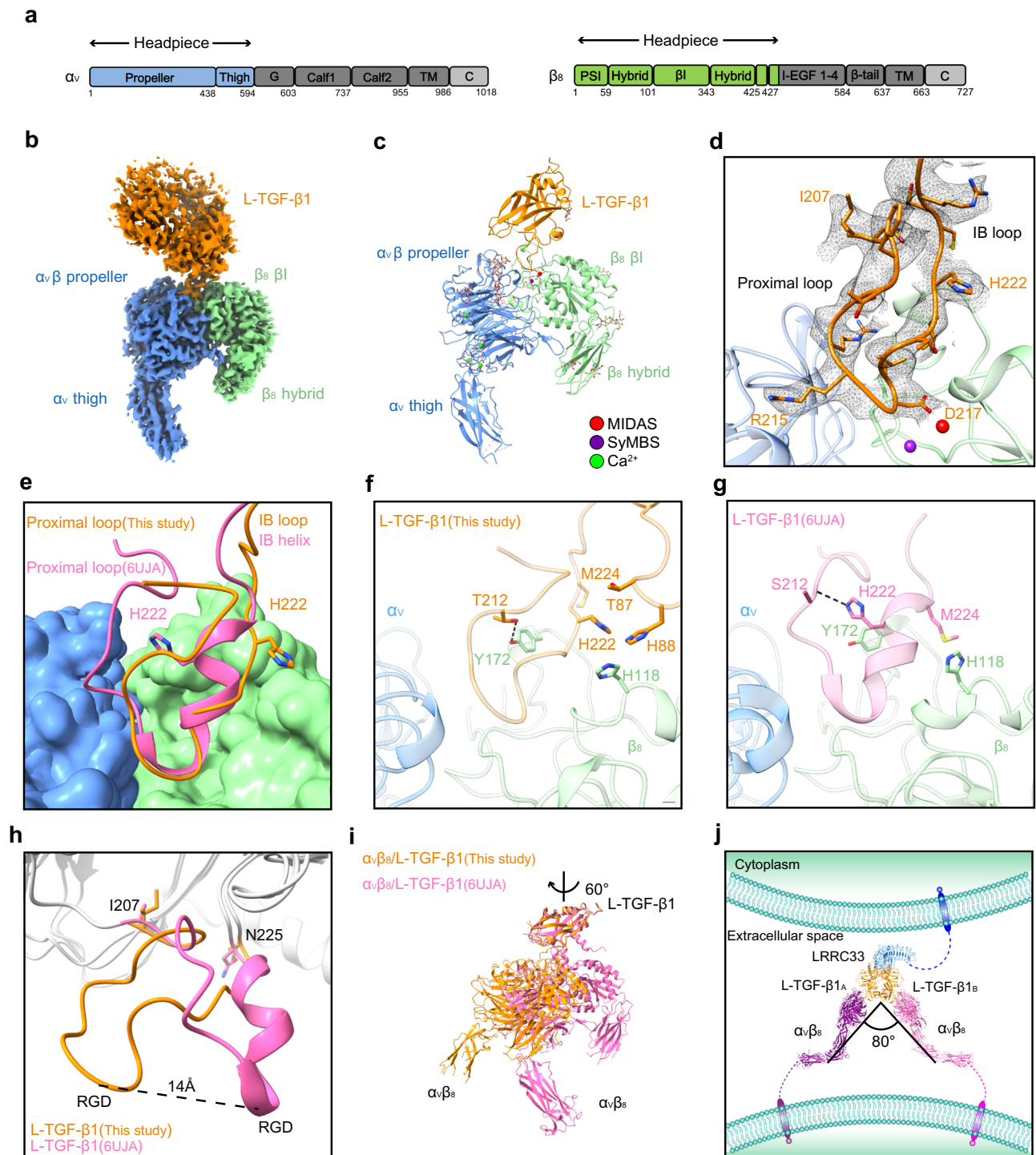


Fig. 3 | Cryo-EM structure of the $\alpha_V\beta_8$ /L-TGF- β 1 complex. **a** Sequence schematic diagrams of integrin subunits α_V and β_8 . The headpiece regions of α_V and β_8 used in our study are colored in blue and green, respectively. The other regions of integrin are colored in gray. **b** Cryo-EM map of the $\alpha_V\beta_8$ /L-TGF- β 1 complex. The contour level is 0.384. The integrin subunits are colored as those in **a**. L-TGF- β 1 is colored in orange. The cryo-EM density of LRRC33 is too weak to visualize. **c** Cartoon presentation of the $\alpha_V\beta_8$ /L-TGF- β 1 structure built in the final model. Metal ions in the MIDAS (metal ion-dependent adhesion site) and SyMBS (syngeneic metal ion binding site) are colored in red and purple, respectively. Calcium ions are colored in green. **d** Ribbon diagram of the interface between $\alpha_V\beta_8$ and L-TGF- β 1. The side chains of the residues in the integrin-binding region of L-TGF- β 1 are shown as sticks, and their cryo-EM densities (contour level of 0.384) are shown as black mesh. The proximal loop and integrin-binding (IB) loop are indicated. **e** Superposition of our $\alpha_V\beta_8$ /L-TGF- β 1 structure with the reported one (PDB code: 6UJA) based on integrin

$\alpha_V\beta_8$. $\alpha_V\beta_8$ is shown in surface presentation, and L-TGF- β 1 is shown in ribbon. L-TGF- β 1 in our structure is colored in orange, and that in the reported structure (PDB code: 6UJA) is colored in pink. The side chains of His222 in these two structures are shown as sticks. **f, g** Detailed comparison of the L-TGF- β 1 integrin-binding regions between the two structures shown in **e**. The residues with distinct conformational changes are shown as sticks. Black dashed lines represent hydrogen bond interaction (<4 Å). **h** Superposition of the L-TGF- β 1 Arm domain between our structure and the reported one (PDB code: 6UJA). The integrin-binding region exhibits a huge conformational difference. Two fixed residues, Ile207 and Asn225, are shown with side chains. **i** Superposition of our $\alpha_V\beta_8$ /L-TGF- β 1 structure with the reported one (PDB code: 6UJA) based on L-TGF- β 1. Integrin $\alpha_V\beta_8$ rotates -60 degrees along the vertical axis. **j** Assembled structural model for the 2:2:1 $\alpha_V\beta_8$ /L-TGF- β 1/LRRC33 complex. The lower leg of integrin α_V (PDB code: 6AVU) is integrated into this model.

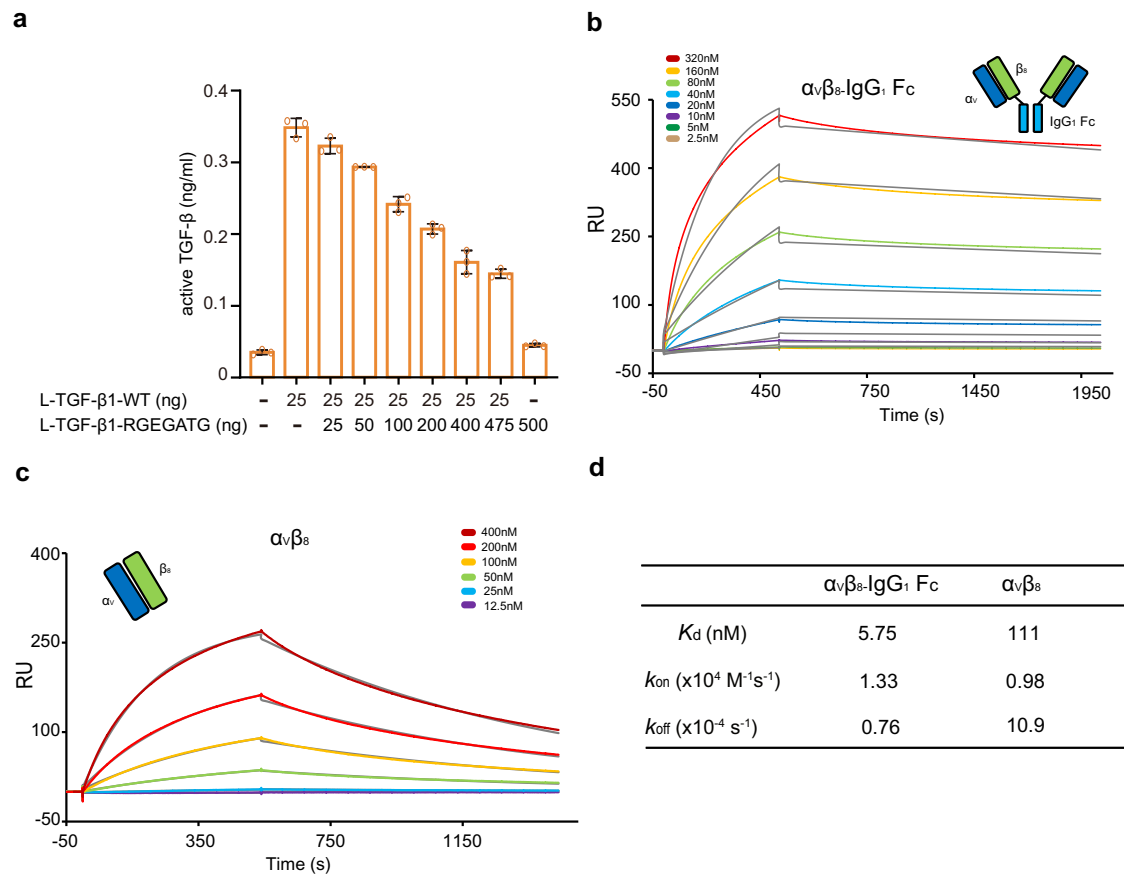


Fig. 4 | Functional significance of the 2:2 binding stoichiometry between integrin $\alpha_V\beta_8$ and L-TGF- β 1. **a** The measured TGF- β 1 activity in (CAGA)₁₂-Luciferase reporter cells when co-cultured with L-TGF- β 1/GARP and integrin $\alpha_V\beta_8$ expressing cells. The controlled amount of WT and integrin-binding defective (RGEGATG) L-TGF- β 1 plasmids was indicated. All experiments were done in triplicate ($n = 3$ biologically independent experiments, mean \pm s.d.). **b, c** The surface plasmon resonance (SPR) results for affinity measurements between L-TGF- β 1 and

two integrin $\alpha_V\beta_8$ variants. Both the experimental (chromatic) and fitting (gray) curves are shown. $\alpha_V\beta_8$ -IgG₁ Fc refers to a heterotetramer of $\alpha_V\beta_8$ linked by IgG₁ Fc fragment. As indicated, the concentrations of integrins used in the experiment were different in the two experiments. **d** Summarization of the dissociation constants (K_d) and kinetic parameters (k_{on} and k_{off}). Source data are provided as a Source Data file.

bind the dimeric L-TGF- β 1 at a 2:2 ratio (Fig. 4b). Surface plasmon resonance (SPR) results showed that the tetrameric integrin $\alpha_V\beta_8$ has much higher affinity for L-TGF- β 1 compared to WT $\alpha_V\beta_8$ (K_d of 5.75 vs. 111 nM, respectively), demonstrating that the 2:2 binding mode indeed increases their binding avidity (Fig. 4b–d). Taken together, our results indicated that the 2:2 binding stoichiometry between integrin $\alpha_V\beta_8$ and L-TGF- β 1 is a biologically relevant state for TGF- β 1 activation.

We then looked into the specificity of L-TGF- β 1 binding to integrins $\alpha_V\beta_6$ and $\alpha_V\beta_8$. Both integrins can activate L-TGF- β 1, but $\alpha_V\beta_6$ has -50-fold higher affinity for L-TGF- β 1 than $\alpha_V\beta_8$ ^{16,17}. As the two integrins share the α_V subunit, the β subunits were examined in detail to

elucidate their specific binding properties for L-TGF- β 1. It has been shown that three specificity-determining loops (SDLs) contribute to the ligand recognition ability of integrin β subunits³⁴. In the β_6 subunit, SDL1 and SDL3 coordinate the conserved binding of ADMIDAS metal ions adjacent to the ligand-binding pocket (Fig. 5a). While the primary sequence and ternary structure of SDL3 are highly conserved between β_6 and β_8 , the negatively charged Asp130 and Asp131 in the SDL1 of β_6 are substituted by Asn119 and Asn120 in β_8 (Fig. 5b), which causes the lack of ADMIDAS metal ions in β_8 (Fig. 5c and Supplementary Fig. 9a). However, simultaneously mutating Asn119 and Asn120 of β_8 to Asp only showed a modest effect on the L-TGF- β 1 affinity of $\alpha_V\beta_8$ ³¹.

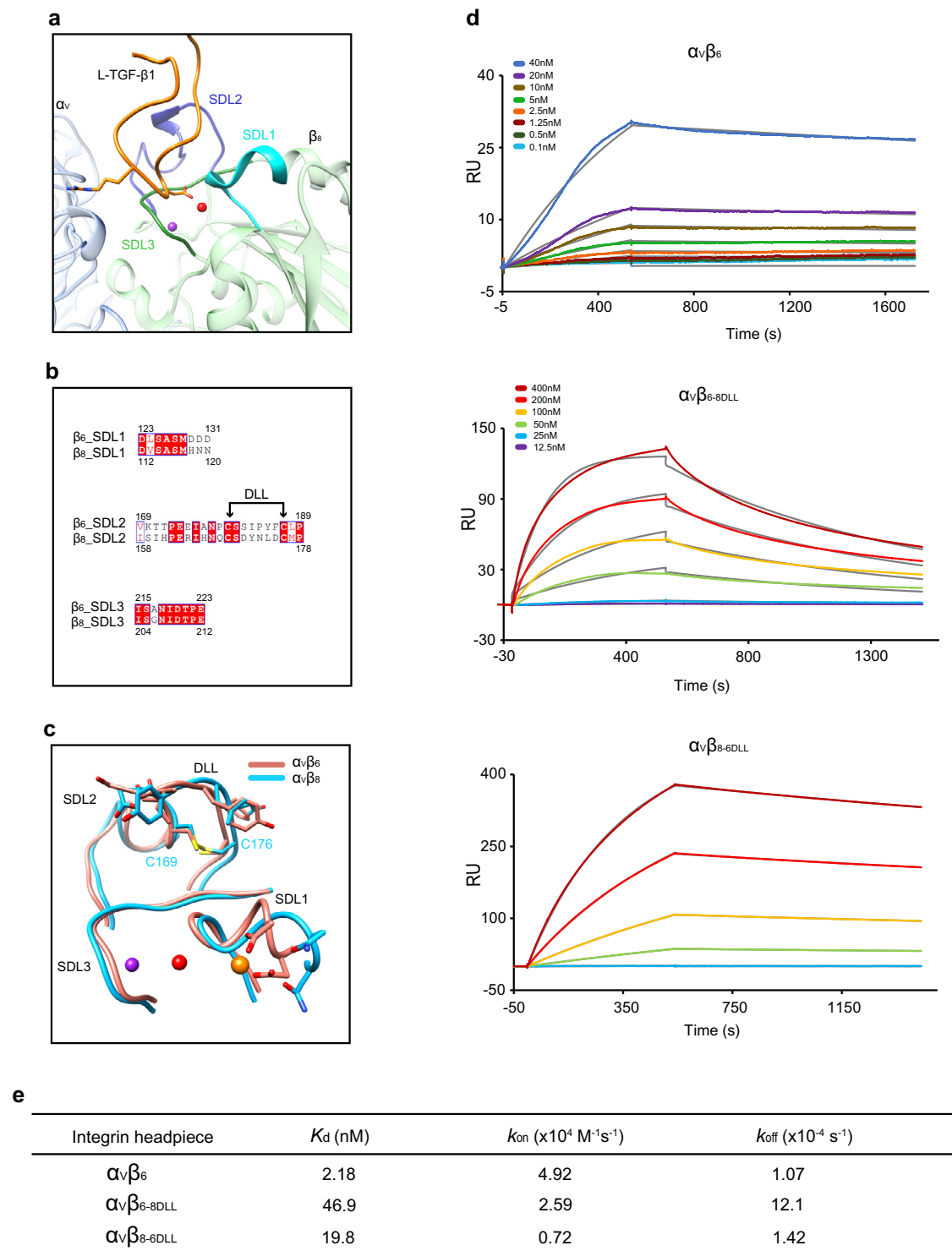


Fig. 5 | Structural and functional analyses of the disulfide-linked loop (DLL) regions of integrin subunits β_6 and β_8 for their contributions to L-TGF- β_1 binding. **a** Ribbon diagram for the specificity-determining loops (SDLs) of $\alpha_v\beta_8$ in the complex structure with L-TGF- β_1 . SDL1, cyan; SDL2, purple; SDL3, dark green. **b** Sequence alignment of the three SDLs between integrin subunits β_6 and β_8 . DLL, disulfide-linked loop. **c** Structural comparison of SDLs in the structures of $\alpha_v\beta_6$ /L-TGF- β_1 (blue) and $\alpha_v\beta_8$ /L-TGF- β_1 (pink, PDB code: 5FFO). **d** The surface plasmon

resonance (SPR) results for affinity measurements between L-TGF- β_1 and different integrin variants. Both the experimental (chromatic) and fitting (gray) curves are shown. $\alpha_v\beta_6$ -8DLL, the DLL of β_6 is substituted by that of β_8 ; $\alpha_v\beta_8$ -6DLL, the DLL of β_8 is substituted by that of β_6 . As indicated, the concentrations of $\alpha_v\beta_6$ used in the experiment were different from those in the other two experiments. **e** Summarization of the dissociation constants (K_d) and kinetic parameters (k_{on} and k_{off}) for the binding between L-TGF- β_1 and different integrin variants.

Therefore, SDL1 and SDL3 of β subunits are unlikely the primary determinant for the different L-TGF- β_1 affinity.

On the other hand, we noted that 5 out of 8 residues of the disulfide-linked loop (DLL) within SDL2 are different between β_6 and β_8

(Fig. 5b). Moreover, although the main chains of DLLs in β_6 and β_8 are similar upon L-TGF- β_1 binding, the side chains of DLLs adopt significantly different conformations (Fig. 5c). We thus swapped the DLL of β_8 to β_6 and prepared the mutant integrin headpiece protein (i.e.,

$\alpha_V\beta_6$ -SDLL), and vice versa (i.e., $\alpha_V\beta_8$ -6DLL). The L-TGF- β 1 affinity of such mutant integrin proteins was then measured by SPR. The WT $\alpha_V\beta_6$ bound L-TGF- β 1 with a K_d value of 2.18 nM, while that of $\alpha_V\beta_8$ was 111 nM, in accordance with the higher binding affinity of $\alpha_V\beta_6$ to L-TGF- β 1. In contrast, the L-TGF- β 1 affinities of mutant $\alpha_V\beta_6$ -8DLL ($K_d = 46.9$ nM) and $\alpha_V\beta_8$ -6DLL ($K_d = 19.8$ nM) were shifted towards that of $\alpha_V\beta_8$ and $\alpha_V\beta_6$, respectively. Interestingly, the k_{off} values were more affected than the k_{on} values (Figs. 4c, d, and 5d, e). It was reported that the headpiece opening of integrin $\alpha_V\beta_6$ contributes to its higher affinity for L-TGF- β 1 than integrin $\alpha_V\beta_8$ that remains in the closed conformation upon L-TGF- β 1 binding. We observed that $\alpha_V\beta_6$ -8DLL and $\alpha_V\beta_8$ -6DLL maintain their intrinsic open and closed conformations in the complexes with L-TGF- β 1, respectively (Supplementary Fig. 11a, b), ruling out the possibility that the DLL swapping between β_6 and β_8 would change the ligand affinity via the effect on their inherent conformational adjustment. Together, the results identified the DLL within SDL2 of β_6 and β_8 as the key determinant for their different affinities for L-TGF- β 1.

Discussion

TGF- β signaling is broadly involved in the development, homeostasis, and diseases^{1,7,22,35–37}. Extensive studies have demonstrated that TGF- β 1, TGF- β 2, and TGF- β 3 exert intrinsically distinct biological activities^{38–40}, although the three isoforms initiate the same downstream signaling events via TGF- β receptors. Moreover, even the same isoform could carry out drastically different functions in different physiological contexts. Consequently, therapeutic applications against the TGF- β pathway has been greatly hindered due to severe adverse side effects caused by blocking TGF- β 's function systematically³⁵. Therefore, uncovering the mechanism designating the specificity of TGF- β signal is central to the biological understanding of the TGF- β pathway.

Recent studies on the activation and extracellular deposition of the latent TGF- β precursor provide an alternative perspective for the mechanisms underlying the functional specificity of TGF- β ^{14–17,19,23,24}. TGF- β is synthesized as a latent form (L-TGF- β). It becomes increasingly evident that specific distribution of L-TGF- β in the extracellular microenvironment and the release of mature TGF- β from the latent form are the two critical checkpoints for the functional divergence of the three TGF- β isoforms. For instance, the anchor proteins LTBP-1 and -3 can present all the three TGF- β isoforms, but LTBP-4 only binds TGF- β 1⁴¹. Therefore, different expression patterns of such LTBPs would help determine the signaling heterogeneity of TGF- β isoforms in various biological contexts⁴². Of importance, LRRC33 is identified as a L-TGF- β anchor protein on the surface of myeloid lineage cells. LRRC33-deficient mice feature impaired TGF- β 1 signaling, resulting in aberrant activation of microglia and multiple neurological disorders in the CNS^{14,43}. In addition, different myeloid cells in the cancer microenvironment, e.g., myeloid-derived suppressor cells, tumor-associated macrophages, and dendritic cells, have been reported to express high levels of LRRC33 and thus to be the major sources of TGF- β 1⁴⁴, whose immunosuppressive function contributes to tumor progression and leads to failure in anti-PD-1/PD-L1 therapies in certain types of cancer⁴⁵.

Notably, LRRC33-deficiency only exhibits TGF- β 1-, but not β 2- or β 3-, related deficits. The mechanism underlying the specific L-TGF- β 1 presentation by LRRC33 and their functional correlation had not been defined until this work. By solving the L-TGF- β 1/LRRC33 complex structure, we showed that LRRC33 only presents L-TGF- β 1 on the cell surface, and revealed that non-covalent interactions between L-TGF- β 1 and LRRC33 are the determinant for their specific pairing. Replacing three key residues on L-TGF- β 2 or - β 3 with the cognate ones of L-TGF- β 1 that mediate such non-covalent interactions was sufficient to enable LRRC33 presentation of these two isoforms (Figs. 2h, i and 6). Moreover, our findings here suggest that cell surface expression of LRRC33 directly correlates with L-TGF- β 1, i.e. it cannot be expressed by itself (Supplementary Fig. 4b, c). These results together indicate that

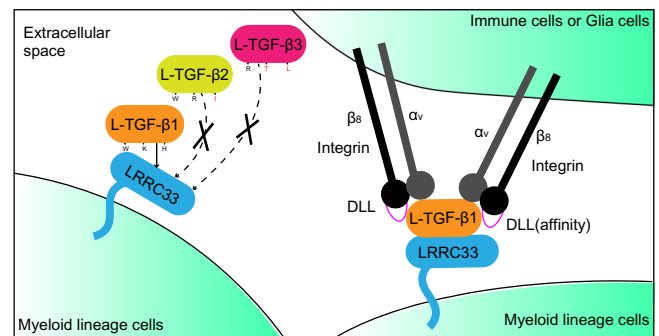


Fig. 6 | Schematic model for the specific TGF- β 1 signal of the myeloid lineage cells designated by LRRC33 and integrin $\alpha_V\beta_8$. The three key residues that determine the specific cell-surface L-TGF- β 1 presentation by LRRC33 are labeled. The cognate residues of L-TGF- β 2 and L-TGF- β 3 are also indicated with the major discriminative ones colored in red.

LRRC33 will be a promising drug target for specifically blocking the myeloid-derived TGF- β 1 signal in therapeutic applications, such as cancer immunotherapy, just like the GARP-targeted TGF- β 1 inhibition for T_{reg} cells⁴⁶. The key non-covalent interaction site we characterized in this work also provides the molecular basis for small molecules design or antibodies development to intervene in L-TGF- β 1 presentation and its subsequent functions.

Unlike TGF- β -expressing non-immune cells, myeloid lineage cells can migrate within tissues and encounter different microenvironments. Therefore, in addition to the specific presentation of the L-TGF- β 1 isoform by LRRC33, mTGF- β 1 release from the latent complex serves as another essential layer of regulation. As aforementioned, activation by $\alpha_V\beta_8$ is more relevant in the context of myeloid lineage cells. The underlying mechanism, however, is still obscure. Both integrins $\alpha_V\beta_6$ and $\alpha_V\beta_8$ binds to the RGDXXL/I motif of L-TGF- β 1, yet it remains unclear how $\alpha_V\beta_6$ and $\alpha_V\beta_8$ exert significantly different ligand affinities. Here we demonstrated it is SDL2 of integrin β subunits that designates their L-TGF- β 1 binding affinities mainly by determining the off-rate (Figs. 4c, d, 5, and 6). Swapping the DLL region of SDL2 between $\alpha_V\beta_6$ and $\alpha_V\beta_8$ could interchange their affinities for L-TGF- β 1. Accordingly, the DLL region of integrins could represent an important entry point for antibodies-mediated targeting of the TGF- β 1 signal.

Another important question in integrin-mediated L-TGF- β 1 activation is the stoichiometry and orientation of their binding. Our 2:2 $\alpha_V\beta_8$ /L-TGF- β 1 complex structure shows a markedly different binding mode compared to the previously reported 1:2 integrin/L-TGF- β 1 complexes^{15,19}. When two $\alpha_V\beta_8$ are bound simultaneously, each integrin rotates 60 degrees along the vertical axis, and forms an 80 degrees angle (Fig. 3i, j). This is in great contrast to the modeled two $\alpha_V\beta_8$ binding pattern based on the 1:2 $\alpha_V\beta_8$ /L-TGF- β 1 complex structure¹⁹, which shows a much larger separation of the two integrins (150 degrees) (Supplementary Fig. 11c). Moreover, the $\alpha_V\beta_8$ /L-TGF- β 1 interface is also different in our 2:2 complex structure. The LATI motif forms a loop (IB loop) instead of the signature α -helical conformation^{17,19,31}, and the buried interface is 19% smaller compared to that of the 1:2 complex (740 Å² vs. 910 Å²)¹⁹. The huge conformational change from the 1:2 to 2:2 $\alpha_V\beta_8$ /L-TGF- β 1 complexes is possibly due to the spatial restrictions of the two integrin-binding motifs residing on the adjacent disulfide-linked bowtie tail loops from each L-TGF- β 1 monomer. Once two integrins bind L-TGF- β 1 concurrently, their local interfaces need to be rearranged to better accommodate each other. Alternatively, it is also possible that the different structures represent two intermediate states in the process of L-TGF- β 1 activation by integrins. Overall, our structural and functional analyses suggest that a 2:2 binding stoichiometry is physiologically relevant. Given the narrow separation and the flexibility of integrin $\alpha_V\beta_8$ legs, two $\alpha_V\beta_8$

integrins on one cell are able to simultaneously bind to one L-TGF- β 1 presented by LRRC33 on a neighboring cell (Figs. 3j and 6). It is possible that the traction force between two adjacent cells provides the mechanical force for LAP dissociation, during which process high avidity caused by simultaneous binding of two α _v β ₈ to one L-TGF- β 1 guarantees the efficient force transmission. In this way, mTGF- β 1 could be released and activates distant cells, not just limited to the L-TGF- β 1 presenting cells¹⁹. Notably, the structural model here was concluded from the truncated headpiece of integrins. As for the full-length α _v β ₈, its interaction mode with L-TGF- β 1 might look different.

In sum, this work identified the mechanism underlying the exquisite specificity of TGF- β 1 presentation and activation, and provided molecular basis for the design of therapeutic agents specifically targeting myeloid-derived TGF- β 1 signal.

Methods

Cell cultures

Sf9 cells (ATCC CRL-1711) were cultured in Sf-900 II SFM medium (Gibco) at 27 °C. HEK293S GnT1⁻ cells (ATCC CRL-3022) were cultured in Yacon HEK293 medium (Yacon Biotechnology) supplemented with 1% fetal bovine serum (FBS) (Vistech) and 100 μ g/ml penicillin/streptomycin (Gibco) at 37 °C with 5% CO₂. Expi293F cells (Gibco A14527) were cultured in OPM-293 CD05 medium (OPM, 81075-001) in suspension or FreeStyle 293 medium (Gibco) adherently at 37 °C with 5% CO₂.

Protein expression and purification

For L-TGF- β 1 and LRRC33, the DNA sequences encoding the full-length L-TGF- β 1 (residues 1–361 excluding signal peptide) and LRRC33 ectodomain (residues 1–631 excluding signal peptide) were cloned into the pEG BacMam expression vector¹⁷. 6 \times His-tag was attached either to the N-terminus of L-TGF- β 1 or the C-terminus of LRRC33. As for integrins, the DNA sequences encoding the headpieces of subunits α _v (residues 1–594 excluding signal peptide), β ₆ (residues 1–474 excluding signal peptide), and β ₈ (residues 1–456 excluding signal peptide) were cloned into the same pEG BacMam vector, and GFP tag was attached to the C-terminus of β subunits. β _{6-8DLL} and β _{8-6DLL} were generated using Gibson assembly protocol. All the plasmids were transformed into DH10Bac *Escherichia coli* competent cells for bacmid generation, and then the recombinant baculoviruses were generated using sf9 insect cells. For the expression of L-TGF- β 1 alone, 10% His-tagged passage 3 (P3) virus was added to HEK293S GnT1⁻ cells at a density of 3 \times 10⁶ cells/ml. For the expression of the L-TGF- β 1/LRRC33 complex and different integrins (α _v β ₆, α _v β ₈, α _v β _{6-8DLL}, and α _v β _{8-6DLL}), equal amount of P3 viruses of untagged L-TGF- β 1 (5%) and His-tagged LRRC33 (5%), or α _v (5%) and the corresponding β subunits (5%), were added together into HEK293S GnT1⁻ cells. 10 mM sodium butyrate was supplemented after 8 h to induce protein expression. The conditioned media were used for protein purification after 3 days' culture.

For protein purification, the conditioned media were first centrifuged at 1700 \times g for 20 min, and then the supernatants were concentrated and exchanged into Buffer A (20 mM Tris pH 8.0 and 500 mM NaCl) using a Hydrosart Ultrafilter system (Sartorius). His-tagged L-TGF- β 1 or L-TGF- β 1/LRRC33 complex were mixed with Ni-NTA beads (Smart-Lifesciences) at 4 °C for 2 h. Next, the beads were washed in turn with Buffer A and B (20 mM Tris pH 8.0, 500 mM NaCl, and 20 mM imidazole) for 20 column volumes (CVs), respectively. Then the proteins were eluted in buffer C (20 mM Tris pH 8.0, 500 mM NaCl, and 200 mM imidazole), followed by cleavage of the his-tag via incubation with PreScission protease at 4 °C overnight. Instead, GFP-tagged integrins were mixed with anti-GFP nanobody (GFPnb)-coupled cyanogen bromide-activated Sepharose beads (GE Healthcare) at 4 °C for 2 h. After washing with Buffer A for 20 CVs, the beads were incubated with PreScission protease at 4 °C overnight to release the target proteins. Finally, all the proteins were further purified by size exclusion

chromatography (SEC) using a Superose 6 Increase 10/300 GL column (GE Healthcare) equilibrated with Buffer D (20 mM HEPES pH 7.5 and 150 mM NaCl). To prepare the 2:2:1 α _v β ₈/L-TGF- β 1/LRRC33 ternary complex, purified integrin α _v β ₈ and L-TGF- β 1/LRRC33 were mixed on ice for 30 min in a molar ratio of 2.2:1 with the addition of 1 mM MnCl₂ and 0.2 mM CaCl₂. Mn²⁺ was used here instead of Mg²⁺ to strengthen the binding of integrin to L-TGF- β 1¹⁶. The extra integrin was removed by another round of SEC in Buffer E (20 mM HEPES pH 7.5, 150 mM NaCl, 1 mM MnCl₂, and 0.2 mM CaCl₂). To prepare the α _v β _{8-6DLL}/L-TGF- β 1 and α _v β _{6-8DLL}/L-TGF- β 1 binary complexes, purified integrins and L-TGF- β 1 were mixed on ice for 30 min in a molar ratio of 2.2:1 with the addition of 1 mM MgCl₂ and 1 mM CaCl₂, followed by SEC in buffer F (20 mM HEPES pH 7.5, 150 mM NaCl, 1 mM MgCl₂, and 1 mM CaCl₂).

Cryo-EM sample preparation and data collection

The protein samples of L-TGF- β 1/LRRC33 and α _v β ₈/L-TGF- β 1/LRRC33 from the peak fractions of SEC were concentrated to 3–4 mg/ml. 3 μ l samples were deposited onto glow-discharged holey-carbon gold grids (Quantifoil), and then blotted, and flash-frozen in liquid ethane using Vitrobot Mark IV (FEI). The blot time was 2 s, humidity was 100%, and temperature was 12 °C.

The grids were first screened using a 200 kV Talos Arctica electron microscope (FEI). The ones in good quality were saved and used for data collection on a 300 kV Titan Krios electron microscope (FEI) equipped with a Gatan imaging filter (20 eV slit). Data acquisition was performed automatically using SerialEM software⁴⁸. All the micrographs were recorded by a K2 Summit direct electron detector (Gatan) in super-resolution mode with a physical pixel size of 1.055 Å. The dose rate was 10 electrons/pixel/second and the total exposure time was 8 s. Each dataset was collected in a single session with a nominal defocus range of 0.8–1.2 μ m. Three datasets were collected for the L-TGF- β 1/LRRC33 sample, which includes 2718, 3031, and 1436 micrographs, respectively. One dataset with 6711 micrographs was collected for the α _v β ₈/L-TGF- β 1/LRRC33 ternary complex.

Cryo-EM data processing

The micrographs were motion corrected using MotionCorr⁴⁹, contrast transfer function (CTF) was estimated using Gctf⁵⁰, and particles were auto-picked using Gautomatch (<http://www.mrc-lmb.cam.ac.uk/kzhang>). The following classifications and refinements were mainly performed in RELION 3.1⁵¹. Non-uniform (NU) and local refinements of cryoSPARC⁵² were carried out for the final refinement.

For the three datasets of L-TGF- β 1/LRRC33, all the extracted particles were combined for data processing. Good classes of 2D classification were input to 3D classification. Then the best classes were combined for 3D auto-refine and produced a 5.10-Å map. A second round of 3D classification without alignment further removed heterogeneous particles and improved the resolution to 4.82 Å. Next, except for a relatively low-resolution class, 5 classes (90.6% particles) from the first round of 3D classification were applied to another round of 3D classification with the 4.82-Å map as reference. From here, the two best classes were selected and refined to 4.74-Å resolution. The two sets of particle stacks that produced the 4.82-Å and 4.74-Å map were then combined and cleaned up by an extra round of 3D classification. The best classes were used for the final refinement. Bayesian polishing and CTF refinement were performed right after to further improve the resolution to 4.66 Å. Then the particles were refined using NU refinement in cryoSPARC, which boosted the resolution to 4.11 Å. Finally, the map was refined to 4.01-Å resolution by implementing a local refinement in cryoSPARC. The post-processed map was generated by DeepEMhancer⁵³.

For the α _v β ₈/L-TGF- β 1/LRRC33 dataset, the 2D classes showed a clear view of 2:2:1 complex. However, 3D classification and auto-refine only generated a 5.19-Å map. To improve the resolution, a mask only containing the 1:2 α _v β ₈/L-TGF- β 1 complex was applied for the

following processing. Two rounds of sequential 3D classification and auto-refine produced a 3.85-Å map. Like the previous dataset, Bayesian polishing, CTF refinement, and the following NU and local refinements finally boosted the resolution to 3.24 Å. Additionally, another round of exquisite 3D classification was performed to verify the plasticity of this complex in our dataset. All the resolutions reported here were calculated using the 0.143 cutoff criterion.

Model building and refinement

The reported structures of $\alpha_V\beta_8$ (PDB code: 6UJA) and L-TGF- β 1 (PDB code: 6GFF) were directly used for our model building, while the initial model of LRRC33 was generated using SWISS-MODEL⁵⁴. All these models were roughly fitted into the cryo-EM maps of L-TGF- β 1/LRRC33 and $\alpha_V\beta_8$ /L-TGF- β 1 using Chimera⁵⁵, then they were manually adjusted using Coot⁵⁶. Refinement of the final structure in real space was done by PHENIX⁵⁷. The geometries of the model were validated using MolProbity⁵⁸. The Fourier shell correlation (FSC) curves were calculated between the refined model and masked full map. Local resolution was estimated in cyroSPARC. All the figures were prepared using Chimera and ChimeraX⁵⁹.

Negative staining EM sample preparation, data collection, and processing

The protein samples of $\alpha_V\beta_{6-8DLL}$ /L-TGF- β 1 and $\alpha_V\beta_{8-6DLL}$ /L-TGF- β 1 from the peak fractions of SEC were diluted to 0.01 mg/ml. 5 μ l samples were deposited onto glow-discharged carbon-coated copper grids (EMCN) for 1 min. The grids were then blotted by filter paper and stained with 2% uranyl acetate. After staining, the grids were dried in air and examined under JEOL JEM-F200 electron microscopy operated at 200 kV. The grids in good quality were used for data collection with a Gatan Oneview camera (Gatan). One dataset with 22 micrographs was collected for $\alpha_V\beta_{6-8DLL}$ /L-TGF- β 1, and another one with 70 micrographs was collected for $\alpha_V\beta_{8-6DLL}$ /L-TGF- β 1. 11,023 particles from the $\alpha_V\beta_{6-8DLL}$ /L-TGF- β 1 dataset and 34,851 particles from the $\alpha_V\beta_{8-6DLL}$ /L-TGF- β 1 dataset were used for 2D classification, respectively.

Surface plasmon resonance (SPR) analysis

The SPR assay was conducted at 25 °C using a Biacore T200 instrument with its inbuild control software (GE Healthcare). WT (C4S/R249A) or mutated (C4S/R249A + RGEATG) L-TGF- β 1 was immobilized on a CM5 chip through amine coupling. Soluble integrin headpieces of $\alpha_V\beta_6$, $\alpha_V\beta_8$, $\alpha_V\beta_{6-8DLL}$, $\alpha_V\beta_{8-6DLL}$, and $\alpha_V\beta_8$ -IgG₁ Fc were prepared in a series of indicated concentrations and injected in turn at a flow rate of 20 μ l/min in HBS buffer (20 mM HEPES pH 7.5, 150 mM NaCl, 1 mM MgCl₂, and 1 mM CaCl₂). The surface was regenerated using 10 mM glycine pH 1.5 by a 30-s pulse (50 μ l/min) at the end of each cycle to restore the resonance units to the baseline. Kinetics analyses were performed using Biacore evaluation software. The experimental data were fitted to a 1:1 Langmuir binding model to generate the kinetics parameters.

L-TGF- β -anchor protein complex formation and surface presentation analysis

Genes encoding N-terminal Flag-tagged GARP and LRRC33 (WT and Y174R) were cloned into pD2529 mammalian expression vector (ATUM). To boost the cell-surface expression of LRRC33, its C-terminal transmembrane domain was substituted with that of GARP¹⁴. Genes encoding L-TGF- β 1, - β 2, and - β 3 (WT and mutants) were cloned into pcDNA3.4 mammalian expression vector (Invitrogen). The flexible furin cleavage site between LAP and the growth factor of L-TGF- β was replaced with HA-tag to prevent dissociation of L-TGF- β and to avoid interfering with complexes formation (N-terminus is involved in complex formation with LRRC33 and GARP, thus N-terminal tagging is not optimal). Mutants were generated by two-step PCR using

PrimeSTAR® HS DNA Polymerase (Takara, R044A) and cloned into Top10 *Escherichia coli* competent cells (Tsingke, TSC-C12) using ClonExpress MultiS One Step Cloning Kit (Vazyme, C113-02). All mutations were validated by DNA sequencing. Transiently transfected Expi293F cells were stained with iFluor 488 conjugated HA antibody (1 μ g/ml, Genscript, Cat A01806, Clone 5E11D8) and iFluor 647 conjugated Flag antibody (1 μ g/ml, Genscript, Cat A01811-100, Clone 5A8E5), and subjected to flow cytometry using a CytoFLEX cytometer (Beckman Coulter). The results were analyzed using FlowJo V10. Supernatants and total lysates of the transfected cells, were subjected to non-reducing and reducing SDS-PAGE for immunoblotting with anti-HA primary antibody (1:2000, Biolegend, Cat 901501, Clone 16B12) and anti-Mouse IgG (whole molecule) HRP secondary antibody (1:30000, Sigma, Cat A9044) to detect L-TGF- β and its complex with LRRC33 or GARP.

L-TGF- β activation assay

Genes encoding L-TGF- β 1 WT with an N-terminal Flag tag and a L-TGF- β 1 variant (RGDLATI->RGEATG) with an N terminal HA tag were cloned into pcDNA3.4 mammalian expression vector. Expi293F cells were transfected with constant amount of GARP (500 ng) and L-TGF- β 1 WT plasmids (25 ng), but gradually increased amount of L-TGF- β 1 variant plasmid (0–475 ng). Transiently transfected Expi293F cells were stained with iFluor 488 conjugated HA and iFluor 647 conjugated Flag antibodies, and analyzed using flow cytometry to determine the cell surface expression of L-TGF- β 1 WT and variant.

5000 transfected cells described above were co-cultured with 5000 integrin $\alpha_V\beta_8$ transfected Expi293F cells and 20,000 Expi293F cells transfected with a TGF- β -SMAD3 responsive (CAGA)₁₂-Luciferase reporter construct. After 24 h of incubation, cells were lysed for 30 min on ice using 50 μ l per well 1 \times Passive Lysis Buffer (Promega, E1941). Then the supernatants were transferred into a 96-well solid white flat microplate (Corning, 3917). 100 μ l luciferase substrate was added per well according to the manufacturer's recommendations (Promega, E1501) and the chemiluminescence was measured using a Synergy H1 microplate Reader (Bio Tek). A standard curve was calculated with serial diluted purified mTGF- β 1 protein (Genscript).

Data availability

The cryo-EM density maps of L-TGF- β 1/LRRC33, integrin $\alpha_V\beta_8$ /L-TGF- β 1 (1:2), and $\alpha_V\beta_8$ /L-TGF- β 1/LRRC33 (2:2:1) have been deposited in the Electron Microscopy Data Bank under the accession codes EMD-33571, EMD-33572, and EMD-33573. The atomic coordinates of L-TGF- β 1/LRRC33 and $\alpha_V\beta_8$ /L-TGF- β 1 have been deposited in the Protein Data Bank under accession codes 7Y1R and 7Y1T. Source data are provided with this paper.

References

- Morikawa, M., Derynck, R. & Miyazono, K. TGF-beta and the TGF-beta family: context-dependent roles in cell and tissue physiology. *Cold Spring Harb. Perspect. Biol.* **8**, <https://doi.org/10.1101/cshperspect.a021873> (2016).
- Mullen, A. C. & Wrana, J. L. TGF-beta family signaling in embryonic and somatic stem-cell renewal and differentiation. *Cold Spring Harb. Perspect. Biol.* **9**, <https://doi.org/10.1101/cshperspect.a022186> (2017).
- Sanjabi, S., Oh, S. A. & Li, M. O. Regulation of the immune response by TGF-beta: from conception to autoimmunity and infection. *Cold Spring Harb. Perspect. Biol.* **9**, <https://doi.org/10.1101/cshperspect.a022236> (2017).
- David, C. J. & Massague, J. Contextual determinants of TGFbeta action in development, immunity and cancer. *Nat. Rev. Mol. Cell. Biol.* **19**, 419–435 (2018).
- Frangogiannis, N. Transforming growth factor-beta in tissue fibrosis. *J. Exp. Med.* **217**, e20190103 (2020).

6. Derynck, R., Turley, S. J. & Akhurst, R. J. TGFbeta biology in cancer progression and immunotherapy. *Nat. Rev. Clin. Oncol.* **18**, 9–34 (2021).
7. Tesseur, I. et al. Deficiency in neuronal TGF-beta signaling promotes neurodegeneration and Alzheimer's pathology. *J. Clin. Invest.* **116**, 3060–3069 (2006).
8. Robertson, I. B. & Rifkin, D. B. Regulation of the bioavailability of TGF-beta and TGF-beta-Related Proteins. *Cold Spring Harb. Perspect. Biol.* **8**, <https://doi.org/10.1101/cshperspect.a021907> (2016).
9. Shi, M. et al. Latent TGF-beta structure and activation. *Nature* **474**, 343–349 (2011).
10. Miyazono, K., Hellman, U., Wernstedt, C. & Heldin, C. H. Latent high molecular weight complex of transforming growth factor beta 1. Purification from human platelets and structural characterization. *J. Biol. Chem.* **263**, 6407–6415 (1988).
11. Wakefield, L. M., Smith, D. M., Flanders, K. C. & Sporn, M. B. Latent transforming growth factor-beta from human platelets. A high molecular weight complex containing precursor sequences. *J. Biol. Chem.* **263**, 7646–7654 (1988).
12. Stockis, J., Colau, D., Coulie, P. G. & Lucas, S. Membrane protein GARP is a receptor for latent TGF-beta on the surface of activated human Treg. *Eur. J. Immunol.* **39**, 3315–3322 (2009).
13. Tran, D. Q. et al. GARP (LRRC32) is essential for the surface expression of latent TGF-beta on platelets and activated FOXP3+ regulatory T cells. *Proc. Natl Acad. Sci. USA* **106**, 13445–13450 (2009).
14. Qin, Y. et al. A Milieu molecule for TGF-beta required for microglia function in the nervous system. *Cell* **174**, 156–171 (2018). e116.
15. Dong, X. et al. Force interacts with macromolecular structure in activation of TGF-beta. *Nature* **542**, 55–59 (2017).
16. Wang, J. et al. Atypical interactions of integrin alphaVbeta8 with pro-TGF-beta1. *Proc. Natl Acad. Sci. USA* **114**, E4168–E4174 (2017).
17. Dong, X. et al. High integrin alphaVbeta6 affinity reached by hybrid domain deletion slows ligand-binding on-rate. *Proc. Natl Acad. Sci. USA* **115**, E1429–E1436 (2018).
18. Mu, D. et al. The integrin alpha(v)beta8 mediates epithelial homeostasis through MT1-MMP-dependent activation of TGF-beta1. *J. Cell Biol.* **157**, 493–507 (2002).
19. Campbell, M. G. et al. Cryo-EM reveals integrin-mediated TGF-beta activation without release from latent TGF-beta. *Cell* **180**, 490–501 (2020). e416.
20. Hinck, A. P., Mueller, T. D. & Springer, T. A. Structural Biology and Evolution of the TGF-beta Family. *Cold Spring Harb. Perspect. Biol.* **8**, <https://doi.org/10.1101/cshperspect.a022103> (2016).
21. Gilbert, R. W. D., Vickaryous, M. K. & Vilorio-Petit, A. M. Signalling by transforming growth factor beta isoforms in wound healing and tissue regeneration. *J. Dev. Biol.* **4**, <https://doi.org/10.3390/jdb4020021> (2016).
22. Travis, M. A. & Sheppard, D. TGF-beta activation and function in immunity. *Annu. Rev. Immunol.* **32**, 51–82 (2014).
23. Zhao, B., Xu, S., Dong, X., Lu, C. & Springer, T. A. Prodomain-growth factor swapping in the structure of pro-TGF-beta1. *J. Biol. Chem.* **293**, 1579–1589 (2018).
24. Lienart, S. et al. Structural basis of latent TGF-beta1 presentation and activation by GARP on human regulatory T cells. *Science* **362**, 952–956 (2018).
25. Saharinen, J., Taipale, J. & Keski-Oja, J. Association of the small latent transforming growth factor-beta with an eight cysteine repeat of its binding protein LTBP-1. *EMBO J.* **15**, 245–253 (1996).
26. Chen, Y. et al. Amino acid requirements for formation of the TGF-beta-latent TGF-beta binding protein complexes. *J. Mol. Biol.* **345**, 175–186 (2005).
27. Walton, K. L. et al. Two distinct regions of latency-associated peptide coordinate stability of the latent transforming growth factor-beta1 complex. *J. Biol. Chem.* **285**, 17029–17037 (2010).
28. Wang, R. et al. GARP regulates the bioavailability and activation of TGFbeta. *Mol. Biol. Cell* **23**, 1129–1139 (2012).
29. Wu, B. X. et al. Glycoprotein A repetitions predominant (GARP) positively regulates transforming growth factor (TGF) beta3 and is essential for mouse palatogenesis. *J. Biol. Chem.* **292**, 18091–18097 (2017).
30. Springer, T. A. & Dustin, M. L. Integrin inside-out signaling and the immunological synapse. *Curr. Opin. Cell Biol.* **24**, 107–115 (2012).
31. Wang, J., Su, Y., Iacob, R. E., Engen, J. R. & Springer, T. A. General structural features that regulate integrin affinity revealed by atypical alphaVbeta8. *Nat. Commun.* **10**, 5481 (2019).
32. Cormier, A. et al. Cryo-EM structure of the alphavbeta8 integrin reveals a mechanism for stabilizing integrin extension. *Nat. Struct. Mol. Biol.* **25**, 698–704 (2018).
33. van Caam, A. et al. TGFbeta-mediated expression of TGFbeta-activating integrins in SSc monocytes: disturbed activation of latent TGFbeta? *Arthritis Res. Ther.* **22**, 42 (2020).
34. Dong, X., Hudson, N. E., Lu, C. & Springer, T. A. Structural determinants of integrin beta-subunit specificity for latent TGF-beta. *Nat. Struct. Mol. Biol.* **21**, 1091–1096 (2014).
35. Akhurst, R. J. & Hata, A. Targeting the TGFbeta signalling pathway in disease. *Nat. Rev. Drug Discov.* **11**, 790–811 (2012).
36. Ciardiello, D., Elez, E., Tabernero, J. & Seoane, J. Clinical development of therapies targeting TGFbeta: current knowledge and future perspectives. *Ann. Oncol.* **31**, 1336–1349 (2020).
37. Heneka, M. T. et al. Neuroinflammation in Alzheimer's disease. *Lancet Neurol.* **14**, 388–405 (2015).
38. Shull, M. M. et al. Targeted disruption of the mouse transforming growth factor-beta 1 gene results in multifocal inflammatory disease. *Nature* **359**, 693–699 (1992).
39. Sanford, L. P. et al. TGFbeta2 knockout mice have multiple developmental defects that are non-overlapping with other TGFbeta knockout phenotypes. *Development* **124**, 2659–2670 (1997).
40. Kaartinen, V. et al. Abnormal lung development and cleft palate in mice lacking TGF-beta 3 indicates defects of epithelial-mesenchymal interaction. *Nat. Genet.* **11**, 415–421 (1995).
41. Saharinen, J. & Keski-Oja, J. Specific sequence motif of 8-Cys repeats of TGF-beta binding proteins, LTBP, creates a hydrophobic interaction surface for binding of small latent TGF-beta. *Mol. Biol. Cell* **11**, 2691–2704 (2000).
42. Annes, J. P., Munger, J. S. & Rifkin, D. B. Making sense of latent TGFbeta activation. *J. Cell Sci.* **116**, 217–224 (2003).
43. Smith, C. et al. Biallelic mutations in NRROS cause an early onset lethal microgliopathy. *Acta Neuropathol.* **139**, 947–951 (2020).
44. Gabrieli, G. et al. Myeloid cell subsets that express latency-associated peptide promote cancer growth by modulating T cells. *iScience* **24**, 103347 (2021).
45. Lan, Y. et al. Enhanced preclinical antitumor activity of M7824, a bifunctional fusion protein simultaneously targeting PD-L1 and TGF-beta. *Sci. Transl. Med.* **10**, <https://doi.org/10.1126/scitranslmed.aan5488> (2018).
46. de Stree, G. et al. Selective inhibition of TGF-beta1 produced by GARP-expressing Tregs overcomes resistance to PD-1/PD-L1 blockade in cancer. *Nat. Commun.* **11**, 4545 (2020).
47. Goehring, A. et al. Screening and large-scale expression of membrane proteins in mammalian cells for structural studies. *Nat. Protoc.* **9**, 2574–2585 (2014).
48. Mastronarde, D. N. Automated electron microscope tomography using robust prediction of specimen movements. *J. Struct. Biol.* **152**, 36–51 (2005).
49. Zheng, S. Q. et al. MotionCor2: anisotropic correction of beam-induced motion for improved cryo-electron microscopy. *Nat. Methods* **14**, 331–332 (2017).
50. Zhang, K. Gctf: Real-time CTF determination and correction. *J. Struct. Biol.* **193**, 1–12 (2016).

51. Fernandez-Leiro, R. & Scheres, S. H. W. A pipeline approach to single-particle processing in RELION. *Acta Crystallogr. D: Struct. Biol.* **73**, 496–502 (2017).
52. Punjani, A., Rubinstein, J. L., Fleet, D. J. & Brubaker, M. A. cryoSPARC: algorithms for rapid unsupervised cryo-EM structure determination. *Nat. Methods* **14**, 290–296 (2017).
53. Sanchez-Garcia, R. et al. DeepEMhancer: a deep learning solution for cryo-EM volume post-processing. *Commun. Biol.* **4**, 874 (2021).
54. Waterhouse, A. et al. SWISS-MODEL: homology modelling of protein structures and complexes. *Nucleic Acids Res.* **46**, W296–W303 (2018).
55. Pettersen, E. F. et al. UCSF Chimera—a visualization system for exploratory research and analysis. *J. Comput. Chem.* **25**, 1605–1612 (2004).
56. Emsley, P., Lohkamp, B., Scott, W. G. & Cowtan, K. Features and development of Coot. *Acta Crystallogr. D: Biol. Crystallogr.* **66**, 486–501 (2010).
57. Adams, P. D. et al. PHENIX: a comprehensive Python-based system for macromolecular structure solution. *Acta Crystallogr. D: Biol. Crystallogr.* **66**, 213–221 (2010).
58. Davis, I. W. et al. MolProbity: all-atom contacts and structure validation for proteins and nucleic acids. *Nucleic Acids Res.* **35**, W375–W383 (2007).
59. Pettersen, E. F. et al. UCSF ChimeraX: structure visualization for researchers, educators, and developers. *Protein Sci.* **30**, 70–82 (2021).

Acknowledgements

The authors thank the Cryo-EM platform and the School of Life Sciences of PKU for cryo-electron microscopy data collection. We are grateful to Zhenxi Guo, Guopeng Wang, Bo Shao, Xia Pei, and Prof. Ning Gao for their help in cryo-EM experiments. We thank Zhaohan Lin and the National Center for Protein Sciences at Peking University for assistance with the SPR experiment. This research was funded by the National Key Research and Development Program of China (NO. 2021YFA1302300 to Z.Z.), the National Natural Science Foundation of China (No. 32171201 to Z.Z.; No. 31971145 to B.Z.; No. 31900867 to J.W.; and No. 32000863 to Y.L.), the Guangdong Zhujiang Talent Program (NO. 2019QN01Y305 to B.Z.), the Shenzhen Science and Technology Program (NO. JCYJ20190807155215221 to B.Z.; and NO. 20200830210645001 to Y.L.), and the Guangdong Provincial Key Laboratory of Digestive Cancer Research (NO. 2021B1212040006 to B.Z.). The study was also supported by Center for Life Sciences (CLS), School of Life Sciences (SLS) of Peking University, the SLS-Qidong innovation fund, Li Ge-Zhao Ning Life Science Youth Research Foundation, and the State Key Laboratory of Membrane Biology of China.

Author contributions

Z.D., J.W., Z.Z., and C.C. purified the protein samples for cryo-EM studies. L.W. purified the mutant L-TGF- β 1 (C4S/R249A) for SPR assay. Z.D., Z.Z., Y.J., and C.C. collected and processed the cryo-EM data. Z.D. and Z.Z. built and refined the structural models. Z.D. and Q.Z. performed the SPR and negative staining EM analyses. X.L. and L.W. carried out flow cytometry and immunoblotting experiments to analyze the expression, secretion, and surface presentation of different L-TGF- β isoforms. C.-H.L. assisted in model building and structural analysis. Z.Z., B.Z., J.Y., Z.D., and J.W. wrote and revised the manuscript with input and support from all co-authors. Y.Q. and Y.L. helped to revise the manuscript.

Competing interests

The authors declare no competing interests.

Additional information

Supplementary information The online version contains supplementary material available at <https://doi.org/10.1038/s41467-022-32655-9>.

Correspondence and requests for materials should be addressed to Bo Zhao, Jianchuan Wang or Zhe Zhang.

Peer review information *Nature Communications* thanks the anonymous reviewer(s) for their contribution to the peer review of this work.

Reprints and permission information is available at <http://www.nature.com/reprints>

Publisher's note Springer Nature remains neutral with regard to jurisdictional claims in published maps and institutional affiliations.

Open Access This article is licensed under a Creative Commons Attribution 4.0 International License, which permits use, sharing, adaptation, distribution and reproduction in any medium or format, as long as you give appropriate credit to the original author(s) and the source, provide a link to the Creative Commons license, and indicate if changes were made. The images or other third party material in this article are included in the article's Creative Commons license, unless indicated otherwise in a credit line to the material. If material is not included in the article's Creative Commons license and your intended use is not permitted by statutory regulation or exceeds the permitted use, you will need to obtain permission directly from the copyright holder. To view a copy of this license, visit <http://creativecommons.org/licenses/by/4.0/>.

© The Author(s) 2022